

In-situ electrochemical study on the effects of Fe(III) on kinetics of pyrite acidic pressure oxidation

Yu Zhang^{1,2} · Can Cui¹ · Sen Lin²  · Heping Li² · Lian Yang¹ · Yadian Xie¹ · Hailiang Hu¹ · Lingyun Zhou¹ · Huanjiang Wang¹ · Chunyan Li¹

Received: 11 December 2023 / Revised: 12 January 2024 / Accepted: 12 March 2024 / Published online: 17 April 2024
© The Author(s), under exclusive licence to Science Press and Institute of Geochemistry, CAS and Springer-Verlag GmbH Germany, part of Springer Nature 2024

Abstract Fe(III) has been proved to be a more effective oxidant than dissolved oxygen at ambient temperature, however, the role of Fe(III) in pyrite acidic pressure oxidation was rarely discussed so far. In this paper, in-situ electrochemical investigation was performed using a flow-through autoclave system in acidic pressure oxidation environment. The results illustrated that increasing Fe(III) concentrations led to raising in redox potential of the solution, and decreased passivation of pyrite caused by deposition of elemental sulfur. Reduction of Fe(III) at pyrite surface was a fast reaction with low activation energy, it was only slightly promoted by rising temperatures. While, the oxidation rate of pyrite at all investigated Fe(III) concentrations increased obviously with rising temperatures, the anodic reaction was the rate-limiting step in the overall reaction. Activation energy of pyrite oxidation decreased from 47.74 to 28.79 kJ/mol when Fe(III) concentration was increased from 0.05 to 0.50 g/L, showing that the reaction kinetics were limited by the rate of electrochemical reaction at low Fe(III) concentrations, while, it gradually turned to be diffusion control with increasing Fe(III) concentrations.

Keywords Pyrite · Pressure oxidation · Fe(III) · In-situ electrochemistry · Hydrothermal experiment

1 Introduction

Pyrite, a significant refractory gold-bearing ore, contains finely dispersed microscopic and ultramicroscopic gold particles within its lattice structure (Yang et al. 2023; Deng and Gu 2022; Xu et al. 2022; Zhuo et al. 2018; Sundarajan et al. 2017; Rabieh et al. 2016; Hazarika et al. 2013; Groudev et al. 1998). As a host mineral, pyrite posed challenges to the efficient extraction of gold through conventional cyanidation methods, necessitating appropriate pretreatment methods to break the crystal lattice of pyrite. The acidic pressure oxidation method has been proposed and continuously improved as an effective pretreatment technique to enhance the gold extraction rate. Specifically, pyrite was pressure oxidized in sulfuric acid solution at high temperatures (above 180 °C) and high oxygen partial pressure as pretreatment before cyanidation (Ng et al. 2022; Yu et al. 2017; Long and Dixon 2004). In 1985, the Homestake Company's McLaughlin gold mine in the United States became the first to commercially treat arsenic-bearing sulfur ore using pressure oxidation, marking a significant milestone in applying this method (Argall 1986).

Papangelakis and Demopoulos (1991) studied the pressure oxidation kinetics of narrow-sized pyrite particulates in the temperature range of 140–180 °C and pressure range 5–20 atm. They proposed that the pressure oxidation of pyrite usually follows the two competitive reactions, as shown in Eqs. (1) and (2). There were three main reactions occurring inside the autoclave under acidic pressure oxidation conditions [Eqs. (1), (3), and (4)]. When the temperature increased, Eq. (1) became predominant, and the generated Fe(II) was subsequently oxidized to Fe(III) by dissolved oxygen, as described in Eq. (4). It could be observed that there was a continuous cycle between Fe(II) and Fe(III) in the oxidation process of pyrite as long as oxygen was present

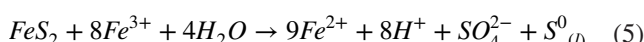
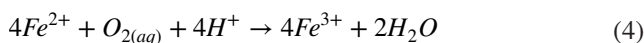
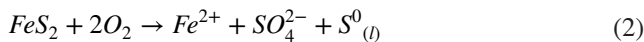
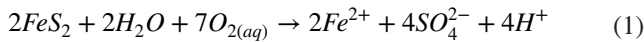
✉ Can Cui
ccals@163.com

✉ Sen Lin
linsen@mail.gyig.ac.cn

¹ School of Chemical Engineering, Guizhou Minzu University, Guiyang 550025, China

² Key Laboratory of High-Temperature and High-Pressure Study of the Earth's Interior, Institute of Geochemistry, Chinese Academy of Sciences, Guiyang 550081, China

in sufficient quantities. The oxidation reactions using Fe(III) as oxidant were shown in Eqs. (3) and (5). It was worth noting that elemental sulfur was produced as a byproduct during the oxidation of pyrite, which would prevent the further oxidation of pyrite (Long and Dixon 2007).



Many researchers have studied the influence of Fe(III) on pyrite oxidation behavior below 100 °C so far. The results demonstrated that Fe(III) was a more effective oxidant than dissolved oxygen. Especially in the solution with a lower pH value, the rate of pyrite oxidation caused by Fe(III) was two orders of magnitude larger than that caused by O₂ (Xu et al. 2016, 2023; Nicol et al. 2018; Huai et al. 2018, 2019; Li et al. 2016, 2017; Zhong 2015). Moses et al. (1987) observed that the decreased oxidation rate of pyrite in the saturated Fe(III) solution was due to the depletion of Fe(III), the quantity of water-soluble Fe(III) supplied to pyrite by Fe(III)-oxyhydroxide was insufficient. It was also proved that the consumption rate of Fe(III) was very fast, especially at the elevated temperatures (Liu et al. 2023). And it was understood that the solubility of ferrous sulphate decreased at high temperatures (Kobylin et al. 2011; Cheng and Demopoulos 2004). Therefore, it was difficult to maintain an appropriate constant concentration of Fe(III) throughout the reaction process to study the kinetic behavior of pyrite acidic pressure oxidation. To our knowledge, very little work on the effect of Fe(III) on pyrite oxidation under acidic high temperature and pressure has been reported. Probably due to the limitations of the closed autoclave, the concentration of Fe(III) couldn't be maintained constant. The present investigation utilized a homemade flow-through autoclave to overcome the limitations of closed autoclaves. The concentration of Fe(III) could remain constant throughout the experiment.

In addition, previous research has indicated that pyrite acidic pressure oxidation is a complex electrochemical process controlled by the surface reaction rate (Liu et al. 2019; Bouffard et al. 2006; Williamson and Rimstidt 1994). Therefore, the research on the kinetic behavior of pyrite during acidic pressure oxidation could be more accurately reflected by using in-situ electrochemical

technology (Cui et al. 2018). In this work, we had innovatively built a flow type high-pressure hydrothermal in-situ electrochemical measurement device, the effects of Fe(III) on kinetics of pyrite acidic pressure oxidation were carried out by in situ electrochemical technology with this system over the temperature range from 160 to 220 °C. The in-situ electrochemical measurements including OCP, EIS, potentiodynamic polarization, and linear polarization curves were used. The results revealed the effects of Fe(III) on the oxidation rate, the passivation phenomenon and the rate-determining step of the oxidation reaction of pyrite.

2 Experimental

2.1 Flow-through autoclave system for in-situ electrochemical measurements

As illustrated in Fig. 1a, experiments were carried out using a flow-through autoclave system. Two high-pressure liquid chromatography (HPLC) pumps were employed to deliver the experimental and reference solutions respectively. The operating pressure was set to 5 MPa using a back pressure valve, and a pressure sensor was employed to monitor the pressure of the system. The mixed solution was collected in the waste tank through the cooler. An electrochemical workstation (Princeton 2263A) was employed for conducting electrochemical analyses.

Figure 1b illustrates the internal piping and electrode system in the flow-through autoclave. The experimental solution was introduced into the autoclave, coming into contact with the pyrite electrode. Subsequently, it converged with the reference solution before being collectively discharged from the autoclave. The thermocouple was positioned at 1–2 mm from the reaction chamber to ensure accurate control of the temperature within the reaction environment. As shown in Fig. 1c, the pyrite electrode (working area 0.28 cm²), which was obtained by cutting large monocrystalline pyrite into a cone frustum, was inserted into the tapered bore at the ceramic electrode base, a PTFE taper sleeve was used to seal the electrode as described in another work of our group (Lin et al. 2017c). The counter electrode was a porous platinum ring sintered onto the ceramic electrode base, the electric signal of the counter electrode was delivered by a platinum wire inside the ceramic electrode base. The reference electrode employed was an external Ag/AgCl electrode. A sapphire glass was placed directly above the pyrite electrode as an optical observation window (Chen et al. 2020). The sapphire glass and the ceramic electrode base were sealed via PTFE O-rings.

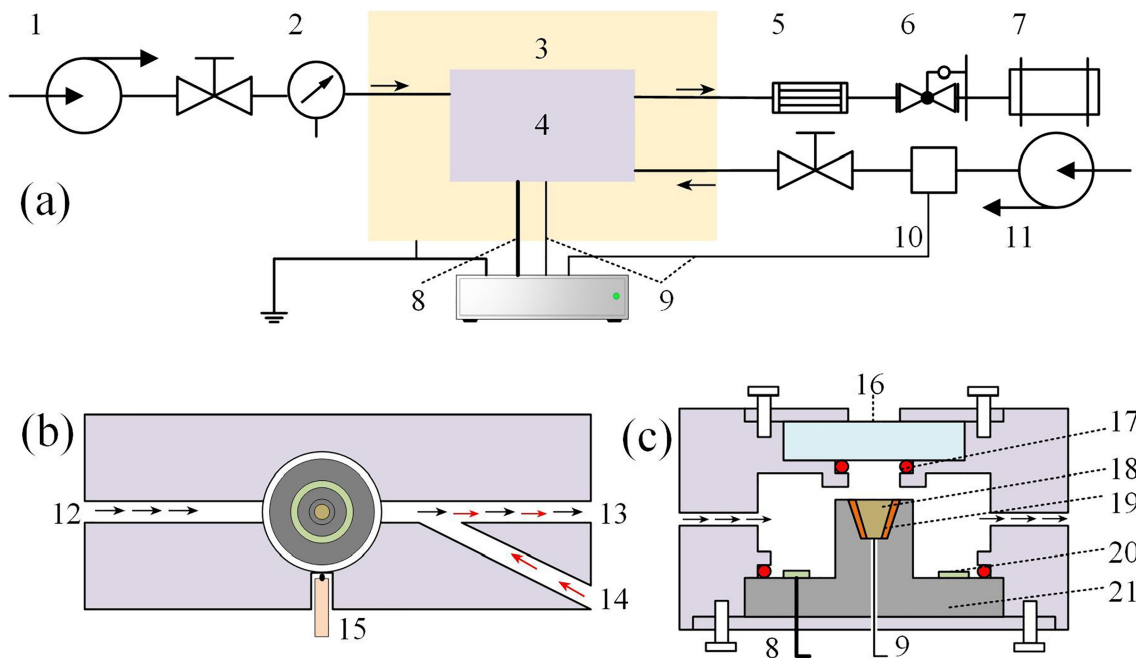


Fig. 1 Schematic diagram of **a** high-pressure hydrothermal experimental system with in-situ electrochemical test and **b** cross section of the autoclave and **c** longitudinal section of the autoclave. Experimental solution pump (1), pressure sensor (2), furnace (3), autoclave (4), cooler (5), back pressure valve (6), waste tank (7), platinum wire (8), silver wire (9), external reference electrode (10), reference solution pump (11), experimental solution (12), mixed solution (13), reference solution (14), thermocouple (15), sapphire window (16), PTFE O-ring seal (17), pyrite electrode (18), PTFE taper sleeve (19), porous platinum film (20), ceramic base (21)

2.2 Experimental materials

The pyrite samples came from Zhaoyuan, Shandong Province, China. Its crystal structure was confirmed by X-ray diffraction. Electron probe analysis showed that the Fe and S contents (in wt%) of the samples were respectively 46.17% and 52.71%, the primary impurity present was SiO₂ (1.06%). Additionally, the main trace elements in the samples were copper (274 ppm), nickel (196 ppm), and cobalt (63.9 ppm). Solutions were prepared using ultrapure water and analytical-grade chemical reagents, which included a 0.3 M sulfuric acid as the experimental solution and a 0.01 M KCl as the reference solution. Specifically, Fe(III) was introduced into the sulfuric acid solution in the form of ferric sulfate, and the Fe(III) concentrations were 0.05, 0.10, 0.20, and 0.50 g/L. Under all experimental conditions, no iron precipitation was found in the autoclave through a high-temperature camera. It was worth emphasizing that the experimental solution needed to be injected into the autoclave first, the reference solution was subsequently pumped only after confirming that the experimental solution had flowed into the waste tank. Regarding the pump speeds, the delivery rate for the experimental solution was set to 1.0 mL/min, while the delivery rate for the reference solution was set to 0.5 mL/min. In this study, all mentioned potentials were standardized concerning the

saturated hydrogen electrode (SHE) using the following formula (Macdonald et al. 1979):

$$\Delta E_{SHE} = \Delta E_{obs} + 286.6 - \Delta T + 1.745 \times 10^{-4} \Delta T^2 - 3.03 \times 10^{-6} \Delta T^3 (mV) \quad (6)$$

2.3 Electrochemical measurements

The working electrode was polished with silicon carbide (SiC) sandpaper ranging from 1000 to 7000 mesh. Following polishing, it was rinsed with distilled water and alcohol. Before injection, the sulfuric acid solution was deoxygenated by purging with argon (99.99%) to eliminate dissolved oxygen. Electrochemical measurements were performed using Princeton 2263A electrochemical station and Powersuite software. Regarding OCP measurements, stability was defined as a potential variation within ± 2 mV over 120 s. The EIS scanning frequency range was configured from 10 kHz to 10 mHz, and EIS data were analyzed using Zsimpwin software (version 3.6). Then, linear polarization curves were generated by scanning in the forward direction from -25 mV versus OCP to 25 mV versus OCP at a scan rate of 0.166 mV/s. Potentiodynamic polarization plots were measured by scanning in the forward direction from -250

mV versus OCP to 750 mV versus OCP at a scan rate of 0.166 mV/s. After each polarization curve measurement, the working electrode was removed and polished to ensure a smooth surface, thereby guaranteeing consistent testing conditions.

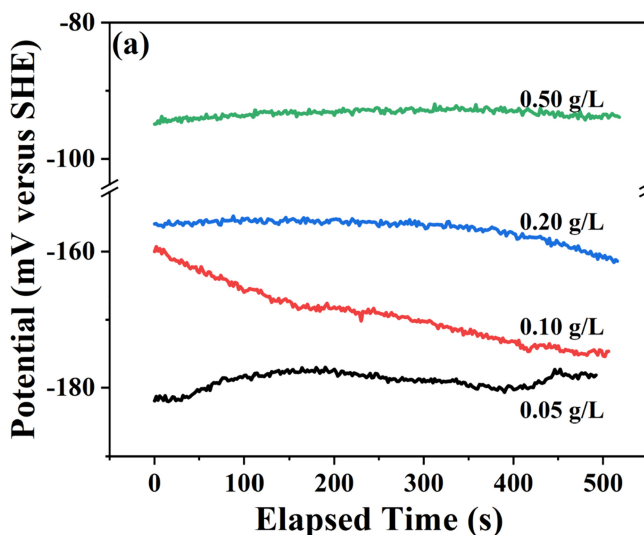
3 Results and discussion

3.1 Open circuit potential analyses

3.1.1 Fe(III) concentration

OCP represented the equilibrium potential of the electrode in an electrochemical system once it reached stability. Figure 2a illustrated the OCP of pyrite in 0.3 M sulfuric acid solution with 0.05, 0.10, 0.20, and 0.50 g/L Fe(III) at 220 °C, 5 MPa. When these Fe(III) were introduced, the following OCP values were measured: −178, −174, −160, and −93 mV, respectively.

The above findings illustrated a clear trend in which increasing Fe (III) concentrations resulted in a progressively positive shift in the OCP. This observation aligned with the findings reported by Sato (1960) and Ahmed (1978), indicating a positive correlation between the OCP of pyrite and the concentration of Fe(III) in the solution. The measured OCP was a mixed potential, which was the coupling of the cathodic reaction with the anodic reaction. The cathodic reaction in the experiments was a reduction of Fe(III):



As the concentration of Fe(III) increased, according to the Nernst equation, the equilibrium potential of the cathodic reaction rose, according to the mixed potential theory, the mixed potential increased accordingly.

3.1.2 Temperature

Figure 2b showed the OCP of the pyrite electrode in 0.3 M sulfuric acid solution with 0.50 g/L Fe(III) at 160–220 °C, 5 MPa. The following OCP values were measured at these temperatures were 158, 67, 30, and −93 mV, respectively. It was observed from Fig. 2b that as temperature increased, OCP values developed more negatively.

OCP acted as an indicator of the corrosion tendency of pyrite. As temperature increased, pyrite and other reactants received an increasing energy supply, making pyrite more susceptible to oxidation (Lin et al. 2017b).

3.2 EIS measurements

3.2.1 Fe(III) concentration

EIS was employed to investigate the impact of experimental conditions on the surface state of pyrite electrode. Figure 3a illustrated a Nyquist diagram of pyrite in 0.3 M sulfuric acid solution with 0.05, 0.10, 0.20, and 0.50 g/L Fe(III) at 220 °C, 5 MPa. The obtained Nyquist plots displayed a flattened semicircle within the experimental frequency range. Furthermore, it was observed that the size of the semicircle diminished with higher concentrations of added Fe(III). Figure 3b displayed the Bode-Z diagram for varying concentrations of Fe(III) at 220 °C. The plot

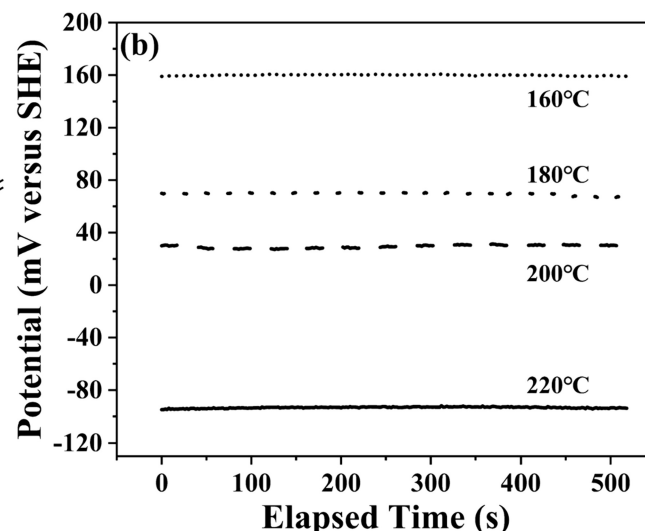


Fig. 2 OCP measurements for pyrite in 0.3 M sulfuric acid solution with **a** 0.05, 0.10, 0.20, and 0.50 g/L Fe(III) at 220 °C, 5 MPa and **b** 0.50 g/L Fe(III) at 160–220 °C, 5 MPa

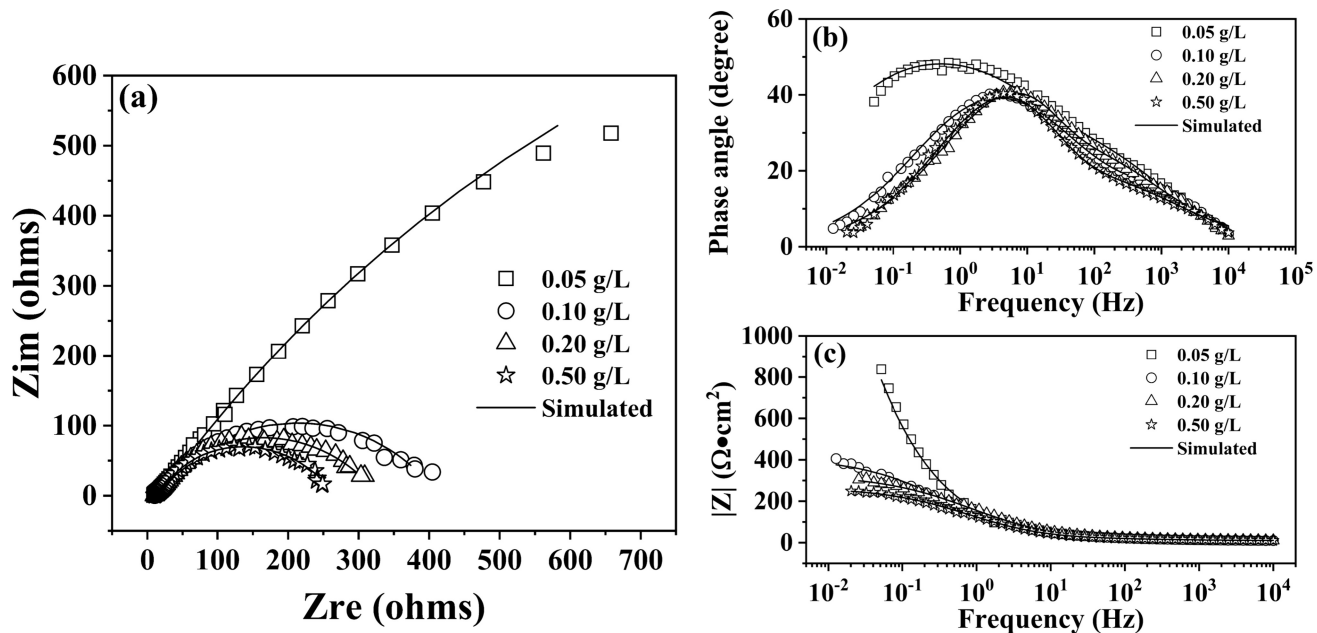


Fig. 3 **a** Nyquist, **b** Bode-Z and **c** Bode-modulus plots of pyrite in sulfuric acid with 0.05, 0.10, 0.20, and 0.50 g/L Fe(III) at 220 °C, 5 MPa

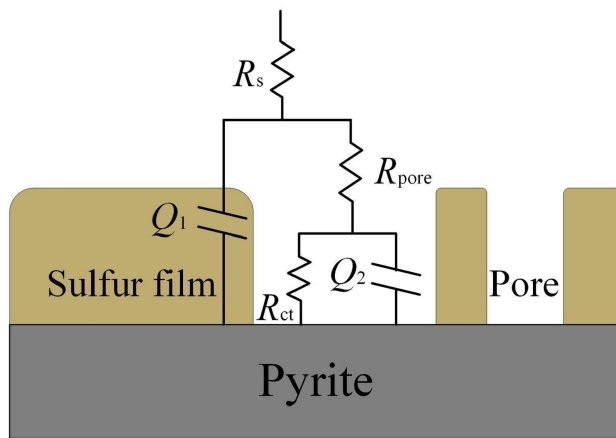


Fig. 4 Equivalent circuit for pyrite in 0.3 M sulfuric acid solution

included two capacitor circuits, indicating two time constants, one appeared in the high-frequency region around 1000 Hz, and another appeared in the low-frequency region below 4 Hz. The high-frequency capacitor circuit

represented the formation of an elemental sulfur layer on the surface of pyrite, which served as a passive film. Conversely, the low-frequency capacitor circuit corresponded to an electric double layer (Liu et al. 2018; Lin et al. 2017a; Deng et al. 2022). Figure 3c exhibited the Bode-modulus diagram for varying concentrations of Fe(III) at 220 °C. The $|Z|$ value associated with a low Fe(III) concentration rapidly increased in the low-frequency region. In contrast, the $|Z|$ value associated with a high Fe(III) concentration exhibited a slower increase.

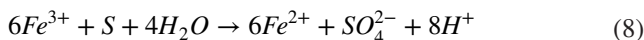
Figure 4 illustrates an equivalent circuit used to fit the experimental results. This circuit was utilized to characterize the surface state of pyrite in sulfuric acid containing Fe(III) under high-temperature and high-pressure conditions (Cui et al. 2018). The circuit was denoted as $R_s(Q_1[R_{\text{pore}}(Q_2R_{\text{ct}})])$. Within this circuit, R_s represented the solution resistance, Q_1 represented the capacitance of the passivation layer, while R_{pore} represented the resistance of the solution within the pore. Q_2 represented the electric double-layer capacitance, while R_{ct} represented the resistance associated with the charge transfer step. Based

Table 1 Equivalent circuit model parameters for pyrite in 0.3 M sulfuric acid with 0.05, 0.10, 0.20, and 0.50 g/L Fe(III) at 220 °C, 5 MPa

$C_{\text{Fe(III)}}$ (g/L)	R_s ($\Omega \cdot \text{cm}^2$)	$Q_1 \cdot Yo \cdot 10^{-4}$ ($S \cdot S^n \cdot \text{cm}^{-2}$)	$Q_1 \cdot n$	R_{ct} ($\Omega \cdot \text{cm}^2$)	$Q_2 \cdot Yo \cdot 10^{-4}$ ($S \cdot S^n \cdot \text{cm}^{-2}$)	$Q_2 \cdot n$	R_{pore} ($\Omega \cdot \text{cm}^2$)
0.05	8.75	17.79	0.57	189	4.14	0.79	3113
0.10	9.62	18.38	0.53	63	2.20	0.90	364
0.20	9.69	13.51	0.57	52	1.89	0.90	268
0.50	9.73	13.96	0.56	23	5.60	0.80	236

on the data presented in Table 1, the values of R_{ct} were determined as 189, 63, 52, and 23 $\Omega \text{ cm}^2$, respectively, at Fe(III) concentrations of 0.05, 0.10, 0.20, and 0.50 g/L. The values of R_{pore} were determined as 3113, 364, 268, and 236 $\Omega \text{ cm}^2$, respectively.

At the same Fe(III) concentration, the values of R_{ct} and R_{pore} obtained from equivalent circuit fitting differed by at least five times, and in some cases, the difference reached one order of magnitude. This might indicate that the charge transfer rate of electrochemical reaction on the electrode surface was relatively fast, while the diffusion rate of reactants and products through the pores of a liquid sulfur layer was slow. As the Fe(III) concentration increased, R_{pore} values decreased by one order of magnitude. The sharp decrease in R_{pore} could be attributed to the following two reasons. Firstly, the equilibrium potential of Fe(III)/Fe(II) represented the redox potential of the solution, increased Fe(III) concentration led to a rise in the redox potential, and it had been provided that sulfur yield in the oxidation product decreased with rising solution redox potential (Flatt and Woods 1995; Chandra and Gerson 2011; Sun et al. 2022). Thus, when Fe(III) concentration was increased, less elemental sulfur was produced in the pyrite oxidation reaction. Secondly, the elemental sulfur deposited on the pyrite surface could also be oxidized by Fe(III) as the following equation:



Increased Fe(III) concentration would accelerate the consumption of the elemental sulfur layer. This observation

aligned with the findings reported by Liu et al. (2011). R_{ct} exhibited the same decreasing trend with increased Fe(III) concentration, indicating that the charge transfer step was accelerated with the expanding supply of the oxidant.

3.2.2 Temperature

Figure 5 shows the EIS of the pyrite electrode in 0.3 M sulfuric acid solution with 0.50 g/L Fe(III) at 160–220 °C, 5 MPa. In Fig. 5a, the change in the radius of the Nyquist plots was relatively tiny with temperature, and there was almost no difference between the Nyquist plots at 200 °C and 220 °C. In Fig. 5b, two-time constants were still observed, with the high-frequency time constant around 3000 Hz and the low-frequency time constant falling within the 3–100 Hz range. Notably, the low-frequency time constant shifted to the left as the temperature increased. In Fig. 5c, the distribution of $|Z|$ in the low-frequency region fell between 250 and 350 $\Omega \text{ cm}^2$. The fitting results in Table 2 revealed that R_{pore} values were at least one order of magnitude higher than R_{ct} at each temperature. When the temperature was increased from 160 to 220 °C, R_{ct} showed a minor decrease from 27 to 22 $\Omega \text{ cm}^2$, R_{pore} decreased from 522 to 236 $\Omega \text{ cm}^2$. The decrease in R_{pore} could be attributed to the fact that rising temperature accelerated the diffusion of liquid sulfur from the pyrite surface into the solution, and the sulfur film thickness on the pyrite surface was decreased, accompanied by expansion of pore diameter within the sulfur film.

The liquid sulfur layer on the pyrite surface, was a crucial factor influencing the acidic pressure oxidation kinetics

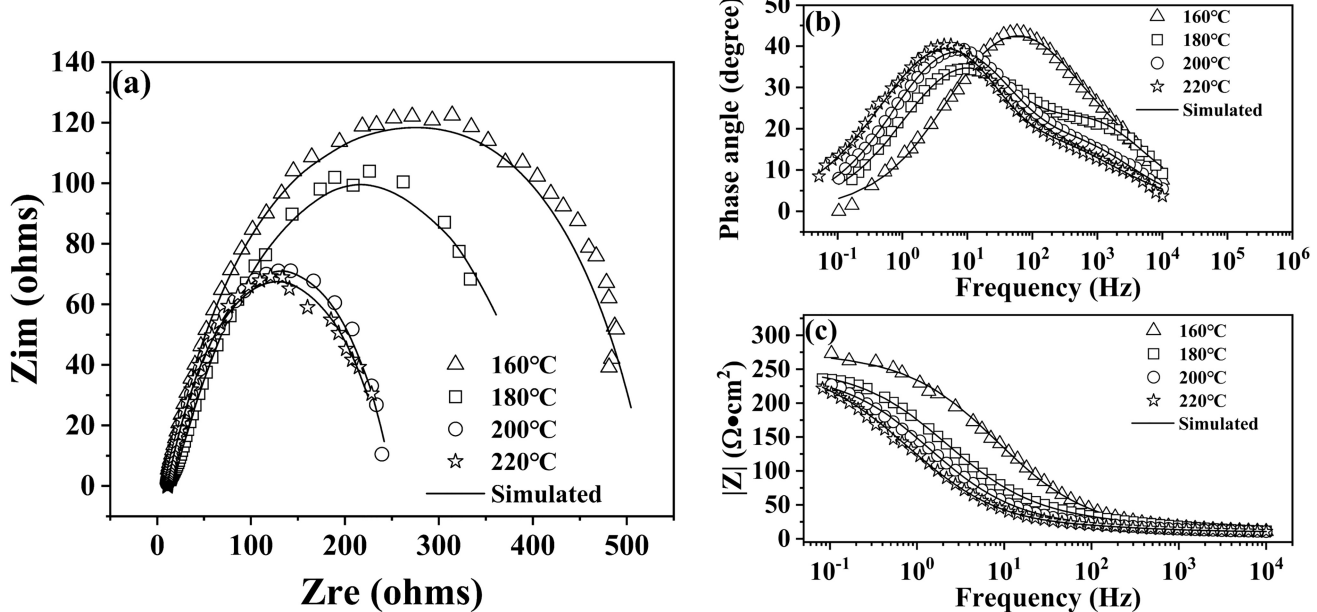


Fig. 5 **a** Nyquist, **b** Bode-Z and **c** Bode-modulus plots of pyrite in sulfuric acid with 0.50 g/L Fe(III) at 160–220 °C, 5 MPa

Table 2 Equivalent circuit model parameters for pyrite in 0.3 M sulfuric acid with 0.50 g/L Fe(III) at 160–220 °C, 5 MPa

Temp (°C)	R_s ($\Omega \text{ cm}^2$)	$Q_1\text{-Yo}$ 10^{-4} ($\text{S S}^\text{n} \text{cm}^{-2}$)	$Q_1\text{-n}$	R_{ct} ($\Omega \text{ cm}^2$)	$Q_2\text{-Yo}$ 10^{-4} ($\text{S S}^\text{n} \text{cm}^{-2}$)	$Q_2\text{-n}$	R_{pore} ($\Omega \text{ cm}^2$)
160	9.08	0.49	0.72	27	0.28	0.41	522
180	11.57	6.29	0.55	24	5.44	0.62	386
200	9.34	10.79	0.55	23	4.09	0.78	240
220	9.73	13.96	0.56	22	5.60	0.80	236

of pyrite. It was in a dynamic balance, on the one hand, elemental sulfur was continuously generated and accumulated onto the pyrite surface. On the other hand, the liquid sulfur layer was also consumed constantly, either oxidized by Fe(III) or diffused into the solution. Both Fe(III) concentration and temperature had varying degrees of impact on the liquid sulfur layer. Higher concentration of Fe(III) promoted the decomposition of the passivation layer, at the same time, reduced the yield of sulfur in pyrite oxidation. The increase in temperature accelerated the diffusion rate of elemental sulfur into the solution.

3.3 Potentiodynamic curve analysis

3.3.1 Fe(III) concentration

Figure 6a illustrated the potentiodynamic polarization curves of pyrite in 0.3 M sulfuric acid solution with 0.05, 0.10, 0.20, and 0.50 g/L Fe(III) at 220 °C, 5 MPa. It could be seen that the potentiodynamic polarization curves moved towards the anodic direction with rising Fe(III) concentrations, the cathodic current densities increased obviously with rising Fe(III) concentrations, while, the

anodic current densities were only slightly changed. It was worth noting that current platforms appeared in the cathodic branches of the potentiodynamic polarization curves, and the current density of the platforms increased with rising Fe(III) concentrations. It should be pointed out that at a Fe(III) concentration of 0.20 g/L, before the appearance of the current platform, there was a slight raising in cathodic current density, and the reason was unknown. The current platforms might represent the limiting diffusion current of the cathodic reaction (Eq. 7). Appearance of limiting diffusion current platforms indicated that the charge transfer step of cathodic reaction was fast, and the reaction was under diffusion control.

The limiting diffusion current density increased with rising Fe(III) concentration, this phenomenon could be explained by Eq. (9):

$$I_L = nFD \frac{C_b}{l} \quad (9)$$

In the formula, n represented the number of electron transfers, F represented the Faraday constant, D represented the diffusion coefficient, C_b represented the Fe(III) concentration in the bulk solution, and l represented

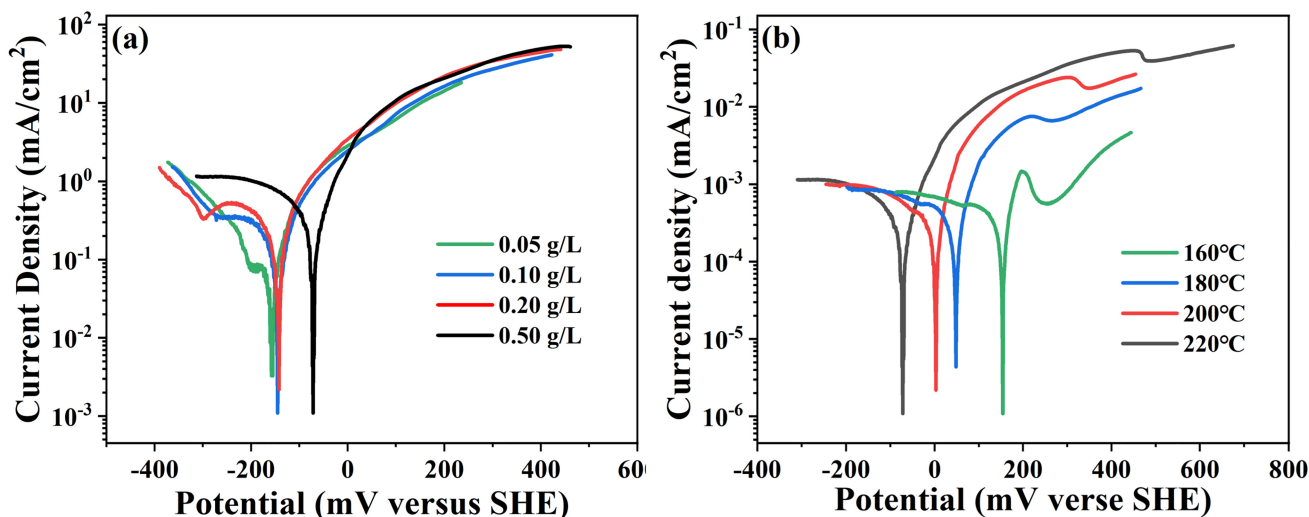


Fig. 6 Potentiodynamic polarization measurements for pyrite in 0.3 M sulfuric acid solution with **a** 0.05, 0.10, 0.20, and 0.50 g/L Fe(III) at 220 °C, 5 MPa and **b** 0.50 g/L Fe(III) at 160–220°C, 5 MPa

the thickness of the stagnant layer. Thus, rising Fe(III) concentrations resulted in higher I_L .

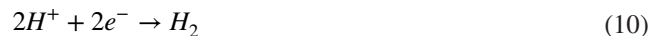
3.3.2 Temperature

Figure 6b presented the potentiodynamic polarization curves of the pyrite in 0.3 M sulfuric acid solution with 0.50 g/L Fe(III) at 160–220 °C, 5 MPa. The potentiodynamic polarization curves moved toward the cathodic direction with rising temperatures. The anodic current densities were elevated significantly at higher temperatures, indicating the anodic reaction, that was oxidation of pyrite, was greatly affected by temperature. While, the cathodic current densities were rarely changed with rising temperatures, the fact revealed that the cathodic reaction, reduction of Fe(III), had a very small activation energy, it was a fast reaction.

The passivation phenomenon appeared in the anodic branches of the potentiodynamic polarization curves, which was caused by the accumulation of elemental sulfur onto pyrite surface during anodic scanning. At 160 °C, the anodic branch entered passivation from 195 mV and ended at 259 mV, with a passivation range of 64 mV. At 180 °C, the anodic branch entered passivation from 217 mV and ended at 267 mV, with a passivation range of 50 mV. At 200 °C, the anodic branch entered passivation from 310 mV and ended at 342 mV, with a passivation range of 32 mV. At 220 °C, the anodic branch entered passivation from 460 mV and ended at 477 mV, with a passivation range of 17 mV. It could be seen that, with rising temperatures, the passivation potential increased, the passivation region was shortened, and the current drop during passivation was also weakened. The phenomenon indicated that elemental sulfur accumulated onto the pyrite surface decreased with rising temperatures. The

possible reason was that rising temperature reduced yield of elemental sulfur during pyrite oxidation (Long and Dixon 2004; Bailey and Peters 1976). Specifically, the diffusion rate of elemental sulfur into bulk solution was enhanced at higher temperatures.

A slight passivation phenomenon was also observed in each cathode branch in Fig. 6b. It was speculated that this was caused by the hydrogen adsorption phenomenon. Pyrite was considered an effective catalyst for hydrogen production reaction (Gou et al. 2020). H^+ could be reduced into hydrogen at pyrite surface, as described in Eq. (10):



Adsorption of hydrogen onto the pyrite surface hindered the reduction of Fe(III), leading to a decrease in cathodic current density.

3.4 Linear polarization curve analysis

Linear polarization curves at various temperatures and Fe(III) concentrations were shown in Fig. 7. The observations and conclusions regarding the corrosion potential in Fig. 7 aligned with those derived from the OCP data. Increased Fe(III) concentration at the same temperature resulted in a higher corrosion potential (Liu et al. 2009). Conversely, when the Fe(III) concentration remained constant, the corrosion potential decreased with rising temperatures. Corrosion current (I_{corr}), which was related to the reaction rate of the pyrite electrode, could be obtained by fitting the Linear polarization curve, the results were shown in Fig. 8. In Fig. 7a, changes in Fe(III) concentration had a noticeable effect on the slope of the polarization curve.

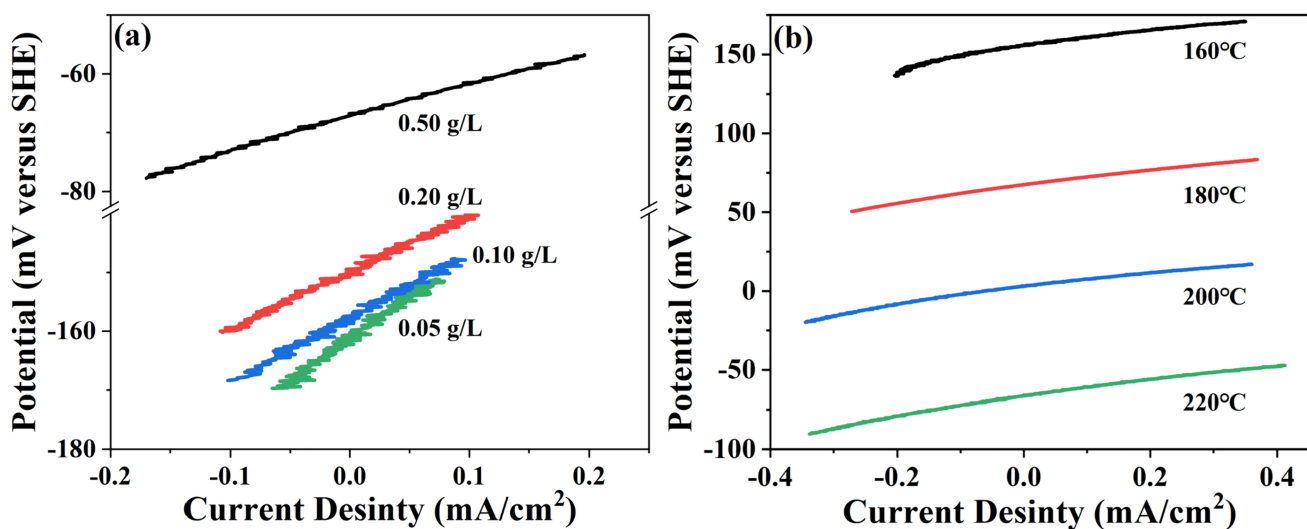


Fig. 7 Linear polarization measurements for pyrite in 0.3 M sulfuric acid solution with **a** 0.05, 0.10, 0.20, and 0.50 g/L Fe(III) at 220 °C, 5 MPa and **b** 0.50 g/L Fe(III) at 160–220 °C, 5 MPa

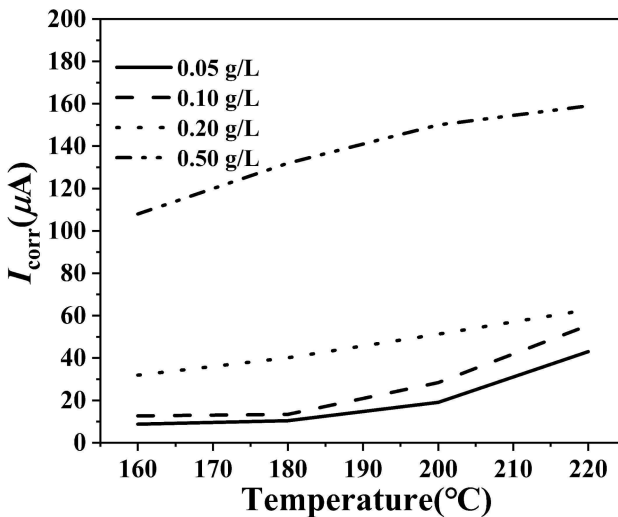


Fig. 8 I_{corr} obtained from Linear polarization data on pyrite in 0.3 M sulfuric acid solution with 0.05, 0.10, 0.20, and 0.50 g/L Fe(III) at 160–220 °C, 5 MPa

Combined with Fig. 8, at a temperature of 220 °C, I_{corr} increased from 43 μA to 159 μA when Fe(III) concentration was increased from 0.05 to 0.50 g/L. In Fig. 7b, the impact of temperature variation on the slope of the polarization curve was less pronounced. Combined with Fig. 8, I_{corr} increased from 108 μA to 159 μA when the temperature changed from 160 to 220 °C.

According to Fig. 8, when the temperature was 160, 180, 200, and 220 °C, as Fe(III) concentration increased from 0.05 to 0.50 g/L, I_{corr} increased by 99, 122, 131, and 116 μA, respectively.

Fe(III) concentration was a primary factor influencing the oxidation rate of pyrite under acidic pressure oxidation conditions. The solubility of Fe(III) was associated with the acidity of the solution, and lower solution pH resulted in higher Fe(III) solubility (Fleuriault et al. 2016; Papangelakis et al. 1994; Dutrizac 1987; Scholten et al. 2019). Predictably, high sulfuric acid concentrations would benefit the oxidation of pyrite, which was provided in previous studies (Craw 2006; Descotes et al. 2004).

The oxidation current density of pyrite was determined by measuring Linear polarization curves in a 0.3 M sulfuric acid solution over a temperature range of 160–220 °C. Fe(III) concentrations were 0.05, 0.10, 0.20, and 0.50 g/L. The apparent activation energy was calculated using the Arrhenius formula:

$$I = A \exp\left(\frac{-E_a}{RT}\right) \quad (11)$$

then,

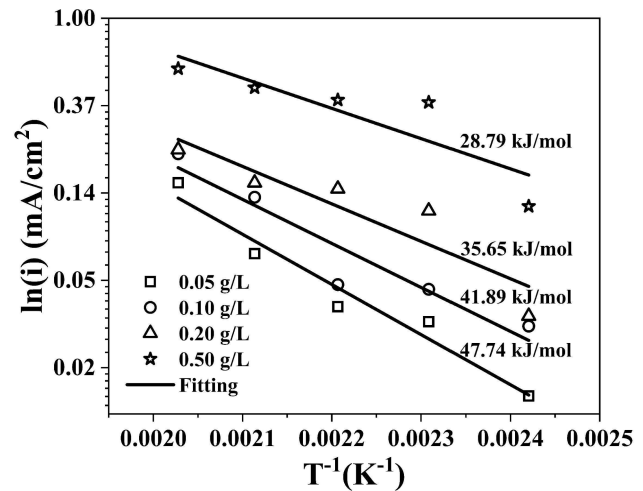


Fig. 9 Arrhenius plots for pyrite in 0.3 M sulfuric acid solution with 0.05, 0.10, 0.20, and 0.50 g/L Fe(III) at 160–220 °C, 5 MPa

$$\ln I = \ln A - \frac{E_a}{RT} \quad (12)$$

finally,

$$E_a = -R \frac{d \ln I}{d(\frac{1}{T})} \quad (13)$$

Figure 9 illustrates the Arrhenius plots for pyrite oxidation in a 0.3 M sulfuric acid solution with varying concentrations of Fe(III). Within the temperature range of 140–220 °C, the E_a values for Fe(III) concentrations of 0.05, 0.10, 0.20, and 0.50 g/L were determined to be 47.74, 41.89, 35.65, and 28.79 kJ/mol, respectively.

Numerous activation energy values for pyrite oxidation have been reported in recent years. Zhong (2015) suggested that the activation energy of the reaction ranges from 33 to 92 kJ/mol, implying that the oxidation process was primarily governed by chemical or electrochemical reactions rather than physical or diffusion reactions. Varying experimental conditions may influence part of the measured activation energy in this experiment. However, it can be demonstrated that decreasing activation energy with an increase in Fe(III) concentration is attributed to the gradual transition to diffusion control of the reaction. Long and Dixon (2004) reported an activation energy value of 33.20 kJ/mol in the temperature range of 170–230 °C. Lin et al. (2017c) discovered that the average activation energy for pyrite oxidation under 40 MPa pressure was 29.80 kJ/mol. Furthermore, Wiersma and Rimstidt (1984) calculated the activation energy at different stirring speeds. They observed that at high stirring speeds, the activation energy was 92 kJ/mol, while at low stirring speeds above 35 °C, it decreased to 25 kJ/mol.

This indicated a change in the reaction mechanism from surface chemical control to mass transfer control. Based on the calculated activation energy, it could be concluded that the primary control mechanism of the reaction shifted from chemical reaction control to mass transfer control with the increase in Fe(III) concentration.

4 Conclusions

The effect of Fe(III) on the acidic pressure oxidation behavior of pyrite was studied by in-situ electrochemical techniques using a flow-through autoclave system in the temperature range of 160 to 220 °C. Several conclusions can be drawn from the results:

1. Higher Fe(III) concentrations accelerated the oxidation of pyrite not only because it acted as oxidant in the reaction, higher Fe(III) concentrations also led to increase in the redox potential of the solution, which resulted in decrease of the passivation phenomenon caused by elemental sulfur.
2. Reduction of Fe(III) at pyrite surface was a fast reaction with low activation energy, it was only slightly promoted by rising temperatures. While, the oxidation rate of pyrite at all investigated Fe(III) concentrations increased obviously with rising temperatures, indicating that the overall reaction was under anode control.
3. Activation energy of pyrite oxidation gradually decreased from 47.74 to 28.79 kJ/mol when Fe(III) concentration was increased from 0.05 to 0.50 g/L. The results showed that the reaction kinetics were limited by the rate of electrochemical reaction at low Fe(III) concentrations, while, it gradually turned to be diffusion control with increasing Fe(III) concentrations.

Acknowledgements This work was financially supported by the Science and Technology Foundation of Guizhou Province, China (No. [2020]1Y163) and the National Natural Science Foundation of China (No. 41827802). The authors would like to acknowledge the Institute of Geochemistry, Chinese Academy of Sciences for the equipment support.

Authors Contribution YZ, CC and SL: Conceptualization, Methodology, Formal analysis, Data curation, Writing—original draft, Writing-review & editing, Funding acquisition; HL: Methodology, Supervision, and Writing-Review & Editing; LY: Resources, Sample collection and Writing-review & editing; YX, HH and LZ: Methodology, Data curation and Writing—review & editing; HW and CL: Visualization, Software and Writing—Review & Editing.

Declarations

Conflict of interests The authors declare that they have no known competing financial interests or personal relationships that could have appeared to influence the work reported in this paper.

References

- Ahmed SM (1978) Electrochemical studies of sulphides, II. Measurement of the galvanic currents in galena and the general mechanism of oxygen reduction and xanthate adsorption on sulphides in relation to flotation. *Int J Miner Process* 5(2):175–182. [https://doi.org/10.1016/0301-7516\(78\)90014-5](https://doi.org/10.1016/0301-7516(78)90014-5)
- Argall OG (1986) Perseverance and winning ways at McLaughlin Gold. *Eng Min J* 187:26–32
- Bailey LK, Peters E (1976) Decomposition of pyrite in acids by pressure leaching and anodization: The case for an electrochemical mechanism. *Can Metall Q* 15(4):333–344. <https://doi.org/10.1179/000844376795050462>
- Bouffard SC, Rivera-Vasquez BF, Dixon DG (2006) Leaching kinetics and stoichiometry of pyrite oxidation from a pyrite–marcasite concentrate in acid ferric sulfate media. *Hydrometallurgy* 84(3–4):225–238. <https://doi.org/10.1016/j.hydromet.2006.05.008>
- Chandra AP, Gerson AR (2011) Redox potential (Eh) and anion effects of pyrite (FeS_2) leaching at pH 1. *Geochim Cosmochim Acta* 75(22):6893–6911. <https://doi.org/10.1016/j.gca.2011.09.020>
- Chen L, Li H, Li S, Xu L, Lin S, Zhou H (2020) Development of *in-situ* Micro-Raman spectroscopy system for autoclave experimental apparatus. *Acta Geochim* 39(4):445–450. <https://doi.org/10.1007/s11631-020-00419-1>
- Cheng TC, Demopoulos GP (2004) Hydrolysis of ferric sulfate in the presence of zinc sulfate at 200 °C: Precipitation kinetics and product characterization. *Ind Eng Chem Res* 43(20):6299–6308. <https://doi.org/10.1021/ie030711g>
- Craw D (2006) Pressure-oxidation autoclave as an analogue for acid–sulphate alteration in epithermal systems. *Miner Depos* 41(4):357–368. <https://doi.org/10.1007/s00126-006-0064-8>
- Cui C, Li H, Lin S, Wang P (2018) In situ electrochemical investigation of acidic pressure oxidation of pyrite at 160–240 °C. *J Electrochem Soc* 165(5):C289–C294. <https://doi.org/10.1149/2.0081807jes>
- Deng S, Gu G (2022) Insight into the influence of mineralogical properties of pristine pyrite on its bioleaching with thermophiles. *Miner Process Extr Metall Rev* 43(6):733–738. <https://doi.org/10.1080/08827508.2021.1931177>
- Deng S, Yan C, Guo K, Gu G (2022) Influence of ferric ions on the electrochemical dissolution behaviors of arsenopyrite in sulfuric acid of pH 1. *Miner Process Extr Metall Rev* 43(6):728–732. <https://doi.org/10.1080/08827508.2021.1931176>
- Descotes M, Vitorge P, Beaucaire C (2004) Pyrite dissolution in acidic media. *Geochim Cosmochim Acta* 68(22):4559–4569. <https://doi.org/10.1016/j.gca.2004.04.012>
- Drutrizac JE (1987) An overview of iron precipitation in hydrometallurgy. Crystallization and precipitation. Elsevier, pp 259–283
- Flatt JR, Woods R (1995) A voltammetric investigation of the oxidation of pyrite in nitric acid solutions: Relation to treatment of refractory gold ores. *J Appl Electrochem* 25:852–856. <https://doi.org/10.1007/BF00233904>
- Fleuriault CM, Anderson CG, Shuey S (2016) Iron phase control during pressure oxidation at elevated temperature. *Miner Eng* 98:161–168. <https://doi.org/10.1016/j.mineng.2016.08.007>
- Gou W, Zhang M, Wu J, Dong Q, Qu Y (2020) Pyrite-type electrocatalysts for hydrogen evolution. *MRS Bull* 45(7):555–561. <https://doi.org/10.1557/mrs.2020.165>
- Groudev SN, Spasova II, Groudeva VI, Ivanov IM (1998) Heap biooxidation: Bioleaching of a refractory gold-bearing ore. *Miner Process*

- Extr Metall Rev 19(1):227–234. <https://doi.org/10.1080/08827509608962442>
- Hazarika P, Mishra B, Saravanan Chinnasamy S, Bernhardt H-J (2013) Multi-stage growth and invisible gold distribution in pyrite from the Kundarkocha sediment-hosted gold deposit, eastern India. *Ore Geol Rev* 55:134–145. <https://doi.org/10.1016/j.oregeorev.2013.05.006>
- Huai Y, Plackowski C, Peng Y (2018) The galvanic interaction between gold and pyrite in the presence of ferric ions. *Miner Eng* 119:236–243. <https://doi.org/10.1016/j.mineng.2018.01.040>
- Huai Y, Plackowski C, Peng Y (2019) The effect of gold coupling on the surface properties of pyrite in the presence of ferric ions. *Appl Surf Sci* 488:277–283. <https://doi.org/10.1016/j.apsusc.2019.05.236>
- Kobylin PM, Sippola H, Taskinen PA (2011) Thermodynamic modelling of aqueous Fe(II) sulfate solutions. *Calphad* 35(4):499–511. <https://doi.org/10.1016/j.calphad.2011.08.005>
- Li L, Polanco C, Ghahreman A (2016) Fe(III)/Fe(II) reduction-oxidation mechanism and kinetics studies on pyrite surfaces. *J Electroanal Chem* 774:66–75. <https://doi.org/10.1016/j.jelecchem.2016.04.035>
- Li L, Bergeron I, Ghahreman A (2017) The effect of temperature on the kinetics of the ferric-ferrous redox couple on pyrite. *Electrochim Acta* 245:814–828. <https://doi.org/10.1016/j.electacta.2017.05.198>
- Lin S, Li H, Cui C (2017a) Electrochemical studies on the corrosion of electrically conductive sulfide minerals in high pressure hydrothermal fluids: A case study from pyrite. *Int J Electrochem Sci* 12(1):610–617. <https://doi.org/10.20964/2017.01.11>
- Lin S, Li H, Xu L, Zhang Y, Cui C (2017b) A novel experimental device for electrochemical measurements in supercritical fluids up to 700 °C/1000 bar and its application in the corrosion study of superalloy Inconel 740H. *RSC Adv* 7(54):33914–33920. <https://doi.org/10.1039/C7RA04054G>
- Lin S, Li H, Xu L, Zhou L, Cui C (2017c) An electrochemical study of pyrite oxidation in 0.1 M sulfuric acid at high temperature and high pressure. *Int J Electrochem Sci* 12(3):1774–1784. <https://doi.org/10.20964/2017.03.68>
- Liu Q, Li H, Zhou L (2009) Experimental study of pyrite–galena mixed potential in a flowing system and its applied implications. *Hydrometallurgy* 96(1–2):132–139. <https://doi.org/10.1016/j.hydromet.2008.09.002>
- Liu Y, Dang Z, Wu P, Lu J, Shu X, Zheng L (2011) Influence of ferric iron on the electrochemical behavior of pyrite. *Ionics* 17(2):169–176. <https://doi.org/10.1007/s11581-010-0492-4>
- Liu Q, Chen M, Zheng K, Yang Y, Feng X, Li H (2018) *In-situ* electrochemical investigation of pyrite assisted leaching of chalcopyrite. *J Electrochim Soc* 165(13):H813–H819. <https://doi.org/10.1149/2.0461813jes>
- Liu Q, Wang S, Chen M, Yang Y (2019) Effect of pyrite on the electrochemical behavior of chalcopyrite at different potentials in pH 1.8 H₂SO₄. *J Chem Res* 43(11–12):493–502. <https://doi.org/10.1177/1747519819873516>
- Liu Y, Xia F, Yang Y, Chen M (2023) Thermodynamic analysis and *in-situ* powder X-ray diffraction investigation of the formation and transformation of mineral phases during pressure oxidation of pyrite. *Hydrometallurgy* 220:106089. <https://doi.org/10.1016/j.hydromet.2023.106089>
- Long H, Dixon DG (2004) Pressure oxidation of pyrite in sulfuric acid media: A kinetic study. *Hydrometallurgy* 73(3–4):335–349. <https://doi.org/10.1016/j.hydromet.2003.07.010>
- Long H, Dixon DG (2007) Pressure oxidation kinetics of orpiment (As₂S₃) in sulfuric acid. *Hydrometallurgy* 85(2–4):95–102. <https://doi.org/10.1016/j.hydromet.2006.08.005>
- Macdonald DD, Scott AC, Wentzke P (1979) External reference electrodes for use in high temperature aqueous systems. *J Electrochim Soc* 126(6):908–911. <https://doi.org/10.1149/1.2129192>
- Moses CO, Kirk Nordstrom D, Herman JS, Mills AL (1987) Aqueous pyrite oxidation by dissolved oxygen and by ferric iron. *Geochim Cosmochim Acta* 51(6):1561–1571. [https://doi.org/10.1016/0016-7037\(87\)90337-1](https://doi.org/10.1016/0016-7037(87)90337-1)
- Ng WS, Liu Y, Chen M (2022) The effect of curing on arsenic precipitation and kinetic study of pressure oxidation of pyrite and arsenopyrite. *Miner Eng* 185:107675. <https://doi.org/10.1016/j.mine.2022.107675>
- Nicol M, Zhang S, Tjandrawan V (2018) The electrochemistry of pyrite in chloride solutions. *Hydrometallurgy* 178:116–123. <https://doi.org/10.1016/j.hydromet.2018.04.013>
- Papangelakis VG, Demopoulos GP (1991) Acid pressure oxidation of pyrite: Reaction kinetics. *Hydrometallurgy* 26(3):309–325. [https://doi.org/10.1016/0304-386X\(91\)90007-9](https://doi.org/10.1016/0304-386X(91)90007-9)
- Papangelakis VG, Blakey BC, Liao H (1994) Hematite solubility in sulphate process solutions. *Hydrometallurgy* 1994. Springer, Dordrecht, pp 159–175. https://doi.org/10.1007/978-94-011-1214-7_9
- Rabieh A, Albijanic B, Eksteen JJ (2016) A review of the effects of grinding media and chemical conditions on the flotation of pyrite in refractory gold operations. *Miner Eng* 94:21–28. <https://doi.org/10.1016/j.mine.2016.04.012>
- Sato M (1960) Oxidation of sulfide ore bodies; 1, Geochemical environments in terms of Eh and pH. *Econ Geol* 55(5):928–961. <https://doi.org/10.2113/gsecongeo.55.5.928>
- Scholten L, Schmidt C, Lecumberri-Sanchez P, Newville M, Lanzirotti A, Sirbescu M-LC, Steele-MacInnis M (2019) Solubility and speciation of iron in hydrothermal fluids. *Geochim Cosmochim Acta* 252:126–143. <https://doi.org/10.1016/j.gca.2019.03.001>
- Sun H-Y, Tan Q-Y, Jia Y, Shu R-B, Zhong S-P, Ruan R-M (2022) Pyrite oxidation in column at controlled redox potential of 900 mV with and without bacteria. *Rare Met* 41(12):4279–4288. <https://doi.org/10.1007/s12598-016-0844-y>
- Sundararajan VA, Li Z, Hu Y, Fu X, Zhu Y (2017) Invisible gold distribution on pyrite and ore-forming fluid process of the Huangshan orogenic-type gold deposit of Zhejiang, SE China: Implications from mineralogy, trace elements, impurity and fluid inclusion studies. *Int J Earth Sci* 106(3):1057–1073. <https://doi.org/10.1007/s00531-016-1353-9>
- Wiersma CL, Rimstidt JD (1984) Rates of reaction of pyrite and marcasite with ferric iron at pH 2. *Geochim Cosmochim Acta* 48(1):85–92. [https://doi.org/10.1016/0016-7037\(84\)90351-X](https://doi.org/10.1016/0016-7037(84)90351-X)
- Williamson MA, Rimstidt JD (1994) The kinetics and electrochemical rate-determining step of aqueous pyrite oxidation. *Geochim Cosmochim Acta* 58(24):5443–5454. [https://doi.org/10.1016/0016-7037\(94\)90241-0](https://doi.org/10.1016/0016-7037(94)90241-0)
- Xu H, Wang Y, Huagn G, Fan G, Gao L, Li X (2016) Removal of quinoline from aqueous solutions by lignite, coking coal and anthracite. Adsorption kinetics. *Physicochem Probl Miner Process* 52(1):397–408
- Xu H, Ye T, Zhang X, Lu L, Xiong W, Zhu Y (2022) Insights into the adsorption mechanism of N-thiourea-maleamic acid on chalcopyrite surface in the flotation separation of Cu-Mo sulfide ores. *J Mol Liq.* <https://doi.org/10.1016/j.molliq.2022.118554>
- Xu H, Tian H, Deng J, Zhuo Q, Cui J, Wang J, Yin Y, Yu P (2023) Review of influence of steric effect on aggregation behavior of fine particles. *Miner Eng* 203:108304.
- Yang M, Wan Q, Nie X, Luo S, Fu Y, Zeng P, Luo W (2023) Depth profiling of arsenian pyrite in Carlin-type ores through wet chemistry. *Acta Geochim* 42(2):256–265. <https://doi.org/10.1007/s11631-022-00591-6>

- Yu Y, Cheng G, Ma L, Huang G, Wu L, Xu H (2017) Effect of agitation on the interaction of coal and kaolinite in flotation. Powder Technol 313:122–128. <https://doi.org/10.1016/j.powtec.2017.03.002>
- Zhong S (2015) Leaching kinetics of gold bearing pyrite in H_2SO_4 – $Fe_2(SO_4)_3$ system. Trans Nonfer Metals Soc China 25(10):3461–3466. [https://doi.org/10.1016/S1003-6326\(15\)63983-8](https://doi.org/10.1016/S1003-6326(15)63983-8)
- Zhuo Q, Liu W, Xu H, Sun X, Zhang H, Liu W (2018) The effect of collision angle on the collision and adhesion behavior of coal

particles and bubbles. Processes 6(11):218. <https://doi.org/10.3390/pr6110218>

Springer Nature or its licensor (e.g. a society or other partner) holds exclusive rights to this article under a publishing agreement with the author(s) or other rightsholder(s); author self-archiving of the accepted manuscript version of this article is solely governed by the terms of such publishing agreement and applicable law.